

The heartbeat of stellar halos: Insights from the stellar halo mass-metallicity relation

Jenny Gonzalez-Jara^{12,*}, Patricia B. Tissera¹², Antonela Monachesi³, Brian Tapia-Contreras¹², Susana Pedrosa⁴, Rosa Domínguez-Tenreiro⁵, and Lucas Bignone⁴

¹ Instituto de Astrofísica, Pontificia Universidad Católica de Chile. Av. Vicuña Mackenna 4860, Santiago, Chile.

² Centro de AstroIngeniería, Pontificia Universidad Católica de Chile. Av. Vicuña Mackenna 4860, Santiago, Chile.

³ Departamento de Astronomía, Universidad de La Serena, Av. Raúl Bitrán 1305, La Serena, Chile.

⁴ Instituto de Astronomía y Física del Espacio, CONICET-UBA, Casilla de Correos 67, Suc. 28, 1428 Buenos Aires, Argentina.

⁵ Departamento de Física Teórica, Universidad Autónoma de Madrid, E-28049 Cantoblanco, Madrid, Spain.

Received September 15, 1996; accepted March 16, 1997

ABSTRACT

Context. The stellar halo mass–metallicity relation (MZhR) has been observed in nearby Milky Way–mass galaxies and explored in numerical simulations. Recent advances in understanding stellar halo assembly, both observationally and theoretically, motivate the investigation of whether the MZhR is already in place at high redshift.

Aims. This work aims to investigate the presence and evolution of the MZhR from redshift $z \approx 3.5$ to $z = 0$, and to identify when galaxies settle on the present-day MZhR.

Methods. We used central galaxies with stellar mass of $\log_{10}(M_{\star,\text{gal}}/M_{\odot}) \in [9 - 11]$ from CIELO cosmological hydrodynamical zoom-in simulations. We identified stellar halos, from $z \approx 3.5$ to $z = 0$, using the AM–E method, focusing on the region between the 1.5 optical radius and the virial radius. The galaxy sample includes stellar halos with $\log_{10}(M_{\star,\text{halo}}/M_{\odot}) \in [8 - 10]$ at $z = 0$. We presented halo cardiograms, a novel approach to studying the assembly history of stellar halos. Using them, we defined a stability time (t_{stable}) as the first time that the median halo metallicity does not change more than ± 0.1 dex with respect to its value at $z = 0$.

Results. CIELO stellar halos reproduce the present-day observed MZhR. At $z \approx 3.5$, stellar halos already define an MZhR whose slope is similar to the slope at $z = 0$. For a fixed stellar halo mass, the metallicity increases ~ 0.21 dex from $z \approx 3.5$ to $z = 0$, reflecting the progressive chemical enrichment provided by the accretion of satellites with diverse masses and different levels of enrichment. When the first stellar halo main contributor (SHMC1) provides a mass fraction at least 20% higher than the remaining contributors, the stellar halo metallicity is set once SHMC1 is fully disrupted (merger time: $t_{\text{merger}}^{\text{SHMC1}}$). This yields a clear correlation between t_{stable} and $t_{\text{merger}}^{\text{SHMC1}}$, with a scatter of 2.2 Gyr driven by the relative importance of the second and third main contributing satellites. Finally, we provide two observational tracers for t_{stable} : t_{90} and a stability time from the age–metallicity relation, t_{AMR} . Using the $t_{\text{stable}} - t_{90}$ relation together with $t_{\text{stable}} \approx t_{\text{merger}}^{\text{SHMC1}}$, we infer that if the bulk of the MW’s stellar halo was built up by a single major merger, we predict its merger time occurring at ~ 7.5 Gyr with a RMS of ~ 2.2 Gyr. While for M31, we inferred a merger time about 1.7 Gyr suggesting that its stellar halo just reached the MZhR at $z = 0$.

Conclusions. Our results suggest that estimating t_{stable} could serve as a proxy for dating the moment at which the stellar halo reaches the present-day MZhR, as well as for dating the last major merger that builds up the stellar halo of galaxies. Additionally, together with an estimation of the merger time of the main contributing satellite, it can provide insights into the relative importance of the second and third contributing satellites.

Key words. Galaxies: abundances - Galaxies: formation - Galaxies: halos

1. Introduction

Chemical elements heavier than helium, commonly referred as metals in astronomy, provide unique insight into the processes that drive the formation and evolution of galaxies (Freeman & Bland-Hawthorn 2002; Matteucci 2012). They are synthesized in stars through thermonuclear reactions and subsequently expelled into the interstellar medium (ISM), polluting the gas that fuels the formation of new generations of stars (Nomoto et al. 2013). The abundance of chemical elements, also known as metallicity, is regulated by the interplay between gas inflows, metal recycling via galactic outflows, star formation, mergers and interactions (Maiolino & Mannucci 2019). As a result, scaling relations between stellar mass and metallicity are naturally expected to

arise and trace the physical processes shaping galaxy evolution (Tinsley 1979).

The gas-phase mass-metallicity relation (MZ_{gR}) is one of the most extensively studied scaling relations for galaxies (Lequeux et al. 1979; Tinsley 1979), which stores information on the level of enrichment of star formation regions. The advent of the Sloan Digital Sky Survey (SDSS, York et al. 2000) provided stellar mass and metallicity measurements in the Local Universe, enabling the determination of the stellar mass-metallicity relation ($MZ_{\star\text{R}}$) for local galaxies (Gallazzi et al. 2005; Kirby et al. 2013). While the MZ_{gR} has been studied for several decades (Lequeux et al. 1979; Tinsley 1979; Tremonti et al. 2004; Lee et al. 2006; Maiolino et al. 2008; Torrey et al. 2019; Sanders et al. 2021; Langeroodi et al. 2023), the $MZ_{\star\text{R}}$ has been less explored in extragalactic sources, in part due to observational challenges. The $MZ_{\star\text{R}}$ reflects the cumulative fossil record of

* E-mail: jagonzalez11@uc.cl

the star formation and assembly histories of galaxies (Gallazzi et al. 2005; Panter et al. 2008; Kirby et al. 2013; Ma et al. 2015; De Rossi et al. 2015; Davé et al. 2017; Trussler et al. 2019; Domínguez-Gómez et al. 2023). Even fewer studies have investigated the stellar halo mass-metallicity relation (MZ_hR, Deason et al. 2016; Harmsen et al. 2017; D’Souza & Bell 2018b; Murphy et al. 2022), which is considered to provide insights into the accretion history of their host galaxy (Robertson et al. 2005; Font et al. 2006; Zolotov et al. 2009; Tissera et al. 2013; D’Souza & Bell 2018b; Monachesi et al. 2019; Smercina et al. 2022). The local MZ_hR has been determined by using observations of some nearby spiral galaxies and the Milky Way (MW) (Harmsen et al. 2017; Smercina et al. 2020; Gozman et al. 2023). As expected, this relation is consistent with more massive stellar halos exhibiting higher metallicities. Studying stellar halos in external galaxies remains a challenge due to their low-surface brightness, but in the near future the Vera Rubin Survey and later the ELT, will enable to extend the detection of stellar halos to more galaxies.

Numerical simulations have played an important role in linking stellar halo properties with their accretion histories, which reported that stellar halos were formed by a significant contribution of accreted satellites and in-situ stars (Zolotov et al. 2009; Tissera et al. 2014; Elias et al. 2018; Monachesi et al. 2019; Pulosoni et al. 2020; Cañas et al. 2020; Rey & Starkenburg 2021; Proctor et al. 2024; Tau et al. 2025a; Gonzalez-Jara et al. 2025).

D’Souza & Bell (2018b) investigated the MZ_hR using Illustris simulations (Vogelsberger et al. 2013; Genel et al. 2014), focusing on galaxies with dark matter halo in the range $\log_{10}(M_{\text{DM}}/M_{\odot}) \in [11, 14]$. Illustris galaxies have a large fraction of in-situ stars at large galactocentric distances, which appear to be incompatible with present GHOSTS observations (Harmsen et al. 2017). However, the relative importance of in-situ stars is still under debate (e.g. Cooper et al. 2015; Tau et al. 2025a; Cooper et al. 2025; Wittig et al. 2025). Hence, D’Souza & Bell (2018b) studied the accreted MZ_hR and reported that the dominant progenitor builds most of the accreted mass and drives the accreted MZ_hR. The scatter in this relation was reported to encode information about the mass of the dominant progenitor and, at a given accreted stellar halo mass, reflects the diversity of accretion histories of the stellar halos. They also found that, at a given accreted stellar mass, high metallicity halos tend to have higher fractions of accreted material contributed by one single massive merger event. Similar findings were later reported by Monachesi et al. (2019) using AURIGA simulations.

Regarding the stellar halo mass assembly, numerical simulations suggest that most of the mass in the MW’s stellar halo is expected to be contributed by a few massive accretion events (Monachesi et al. 2019; Pu et al. 2025) along with in-situ stars that are more frequent in the inner stellar halo (Zolotov et al. 2009; Purcell et al. 2010; Tissera et al. 2013; Font et al. 2020). A simulated reconstruction of the assembly of stellar halos beyond MM-like galaxies was presented in Gonzalez-Jara et al. (2025) (hereafter GJ25). These authors focused on the outer halo, excluding the inner region of the halos that coexist with the host galaxy, with stellar masses in the range of $\log_{10}(M_{\star, \text{halo}}/M_{\odot}) \in [8, 10]$ from the CIELO simulations (Tissera et al. 2025). Their results indicate that as the stellar halo mass increases, so does the number of significant progenitors, which in general, contribute more than 60% of the outer halos.

Satellite galaxies that contribute to the formation of stellar halos follow a MZ_hR (Fattahi et al. 2020; Naidu et al. 2022; Khoperskov et al. 2023; Grimozzi et al. 2024). Disrupted dwarf galaxies, in particular, tend to be less metal-rich than surviving satellites at fixed stellar mass. This difference reflects their dis-

tinct star formation timescales, with surviving systems typically sustaining star formation for longer periods (Tissera et al. 2012). If the MZ_hR evolves with lookback time, the stellar halos might inherit a similar trend given they are mainly built from accreted stars from dwarf galaxies.

Recent observations from the CLAUDS and HSC-SSP surveys have enabled the investigation of stellar halo assembly in the redshift range $0.2 \leq z \leq 1.1$ (Williams et al. 2024). These efforts, along with advances in numerical simulations, reveal that low- and high-mass stellar halos exhibit different rates of mass growth (Amorisco 2017; Elias et al. 2018; Tau et al. 2025a; Gonzalez-Jara et al. 2025), largely driven by differences in their accretion histories. If stellar halos evolve through distinct phases of growth and quiescence, it remains to be understood when the MZ_hR first emerges, how it evolves over time, and what information this relation encodes about the assembly history of stellar halos and their host galaxies. The advancement of observational data prompts us to explore these questions further using simulations which include galaxies of a variety of stellar masses.

In this paper, we use the CIELO simulations to investigate the MZ_hR across cosmic time. We use the set of galaxies and their stellar halos studied by GJ25 and analyzed their assembly histories following their progenitors back in time up to $z \approx 3.5$. We compared our simulated halos with available observations at $z \sim 0$ by applying a similar procedure and radial aperture. However, to understand the assembly of the stellar halos and the evolution of the MZ_hR, we focus on the whole stellar halos beyond the region where it coexists with its host galaxy. We extend previous numerical studies beyond the MW-mass halos. We aim to understand when a stellar halo of a galaxy reaches the local MZ_hR and what features of its assembly history are stored in the MZ_hR, its dispersion, and evolution. We present halo cardiograms, a novel approach to study the assembly of stellar halos, and we propose a way to build observables cardiograms.

The paper is organized as follows. Section 2 briefly describes the CIELO simulations and the definitions adopted throughout this work. Section 3 compares the MZ_hR at $z = 0$ using current observations and simulations. Section 4 investigates the stellar halo mass and metallicity from redshift $z \approx 3.5$ to $z = 0$. In Section 5, we introduce cardiograms of stellar halos as an approach to study the halo assembly and we identify when the median halo metallicity is stabilized, i.e. does not change more than ± 0.1 dex respect to its value at $z = 0$. In Section 6, we present observational measurements as proxies to estimate the stability time. Finally, in Section 7 we discuss our results and caveats, followed by a summary in Section 8.

2. Methodology

In this section, we introduce the CIELO simulations (Sec. 2.1) used in this work and describe the adopted definitions (Sec. 2.2) for identifying stellar halos, their stellar populations, and contributing satellites.

2.1. CIELO Simulations

The CIELO simulations are fully cosmological hydrodynamical zoom-in simulations that assume a Λ Cold Dark Matter universe with $\Omega_0 = 0.317$, $\Omega_{\Lambda} = 0.682$, $\Omega_B = 0.049$, $h = 0.671$, $\sigma_8 = 0.834$, $n_s = 0.962$ (Planck Collaboration et al. 2014). The CIELO galaxies are embedded within zoom-in regions, which include small groups, walls, and filaments (Tissera et al. 2025).

The CIELO suite includes two levels of resolution: L11 with $m_{\text{dm}} = 1.36 \times 10^6 M_{\odot} h^{-1}$ and $m_{\text{gas}} = 2.0 \times 10^5 M_{\odot} h^{-1}$ and L12

with $m_{\text{dm}} = 1.36 \times 10^5 M_{\odot} h^{-1}$ and $m_{\text{gas}} = 2.1 \times 10^4 M_{\odot} h^{-1}$. These simulations were run using a version of GADGET-3, an updated version of GADGET-2 (Springel & Hernquist 2003; Springel 2005). This version includes a multiphase model for the ISM, metal-dependent radiative cooling, stochastic star formation, and energy and feedback by Type Ia and II supernovae (SNIa and SNIi, respectively) as described in Scannapieco et al. (2005, 2006). The chemical isotopes included in the simulation are the following twelve: H, ^4He , ^{12}C , ^{14}N , ^{16}O , ^{20}Ne , ^{24}Mg , ^{28}Si , ^{32}S , ^{40}Ca , ^{56}Fe , and ^{62}Zn (Mosconi et al. 2001). The multiphase and SN feedback models are able to trigger violent galactic mass-loaded winds without introducing mass-scale parameters (Scannapieco et al. 2008).

The simulated galaxies are identified using a friends-of-friends algorithm (FoF; Davis et al. 1985) and the SUBFIND algorithm (Springel et al. 2001; Dolag et al. 2009). The merger trees were built using the AMIGA method (Knollmann & Knebe 2009).

The CIELO simulations have been used in previous studies to investigate the effects of the environment on infalling satellite galaxies (Rodríguez et al. 2022), the impact of baryons on the shape of dark matter halos (Cataldi et al. 2023), metallicity profiles of galaxies (Tapia et al. 2022; Tapia-Contreras et al. 2025), primordial black holes as a possible component of the dark matter content (Casanueva-Villarreal et al. 2024), the formation channels of stellar halos (GJ25), the mass-metallicity relation of bulges (Muñoz-Escobar et al. 2025) and metal-loaded outflows in low-mass galaxies (Miranda et al. 2025).

2.2. Sample and definitions

In this work, we analyze 28 stellar halos with $\log_{10}(M_{\star, \text{halo}}/M_{\odot}) \in [8, 10]$ from CIELO simulations, the sample was introduced in GJ25. Our sample spans stellar masses of $\log_{10}(M_{\star, \text{gal}}/M_{\odot}) \in [9, 11]$ and dark-matter halo masses of $\log_{10}(M_{\text{DM}}/M_{\odot}) \in [10, 12]$. The half-mass radii of our galaxies range from ~ 1 to ~ 5 kpc, and the virial radii, r_{vir} , from ~ 80 to 240 kpc¹. Following the same procedure used by GJ25, the stellar components of each galaxy were identified by using the AM-E method described by Tissera et al. (2012), based on the angular momentum and the binding energy of the stellar particles. Briefly, stellar particles that do not belong to the bulge and disk components are considered to be part of the stellar halo.

Following GJ25, we focus on the stellar halo region between $1.5r_{\text{opt}}$ ² and r_{vir} . The inner region of stellar halos, where the stellar halo coexist with its host galaxy, will be discussed in a separate paper.

In order to study the evolution of stellar halos, we traced the 28 halos back in time using the merger trees. Stellar masses and metallicities are estimated up to $z \approx 3.5$ using the aforementioned dynamical decomposition. We adopted a lower limit for the stellar halo mass determined by the numerical resolution of our simulations, considering only stellar halos with more than 500 stellar particles at each analyzed redshift. This corresponds

to a stellar mass limit of $\sim 5 \times 10^6 M_{\odot}$ and $\sim 5 \times 10^7 M_{\odot}$ for the resolution levels L12 and L11, respectively.

We classified present-day stellar halo stars into three categories based on their formation site: in-situ, endo-debris, and ex-situ. A detailed characterization of these populations is given in GJ25. Briefly, in-situ stars were born bound to the central galaxy. Endo-debris stars were mainly formed during wet mergers, bound to a subhalo within the virial radius of the host galaxy. Ex-situ stars were born in another galaxy, located outside the virial radius of the host galaxy, and were later accreted. Since both ex-situ and endo-debris stars originate from accreted material, we define the accreted stellar component as the combination of these two populations.

We define the stellar halo main contributors (SHMCs) as the satellite galaxies that contribute the highest stellar mass to the accreted stellar halo, including both ex-situ and endo-debris stars. We rank them according to their relative contribution (SHMC1, SHMC2, etc.). The infall time, t_{infall} is defined as the lookback time of the last snapshot before the satellite crosses the virial radius of the central galaxy. If a satellite enters more than once, then we consider the first time it does so. The merger time, t_{merger} , is defined as the lookback time of the snapshot when the satellite is no longer recognized as a separate structure and is considered bound to the central galaxy, according to the merger tree.

3. The Local Stellar halo mass metallicity relation

As a first step, we calculated the local CIELO MZhr and compared it with available observations. Figure 1 presents the observed MZhr at $z = 0$ from the GHOSTS survey (black stars, Harmsen et al. 2017; Gozman et al. 2023) and predictions for the accreted stellar halo component from simulations and a semi-analytical model (Murphy et al. 2022, pink hexbins). In addition, we display the median metallicity of the halo between $1.5r_{\text{opt}}$ to r_{vir} (orange squares) considering both the accreted and in-situ populations. These estimations correspond to the stellar populations we will focus on this work. Hence, we include them to have a reference of their level of enrichment.

Stellar metallicities reported by Harmsen et al. (2017) were inferred along the projected minor axis of the disk at a galactocentric radius of 30 kpc, using red giant branch stars in nearby spiral galaxies. The total stellar halo mass was estimated as three times³ the mass enclosed between two ellipses at minor axis radii of 10 and 40 kpc. To mimic these observational constraints, Monachesi et al. (2019) measured the median metallicities at 30 kpc along the minor axis of the Auriga halos, while the halo mass was computed as three times the stellar mass beyond 1.5 optical radii along the major axis and 10 kpc above the disk plane. They estimated both quantities by selecting only the accreted component, i.e., all stars formed in satellites, regardless of whether the satellite was inside or outside the virial radius (gray triangles). Figure 1 also shows stellar halos from the semi-analytic model L-Galaxies 2020-MM (pink hexagons, Murphy et al. 2022), which are assembled only from accreted satellites, thereby containing exclusively ex-situ stars by definition. This model includes thousands of MW analog galaxies, and their metallicities are rescaled at 30kpc. Finally, and following a similar procedure used by Monachesi et al. (2019), the stellar mass of CIELO stellar halos was estimated as three times the mass of accreted stars in the stellar halo within a spherical shell of 10 – 40 kpc. The median metallicity is computed in a 3-

¹ We define r_{vir} as the radius enclosing the overdensity of 200 times the critical density of the Universe, including baryons and dark matter. This was done at all analyzed redshift. In our previous work, GJ25, we used the r_{vir} calculated by the Rockstar halo finder, which considered only dark matter (see Table 1 of GJ25 which displays distances in kpc/h).

² The r_{opt} is defined as the radius that enclosed about 80 percent of the stellar mass of a galaxy. For our galaxies, $1.5r_{\text{opt}}$ ranges from 4.23 to 17.02 kpc.

³ The factor of three is derived from comparisons with theoretical models (Bullock & Johnston 2005; Bell et al. 2017)

dimensional bin around 30 ± 1 kpc of the accreted halo, i.e., stars born in satellites regardless of whether they are inside or outside the virial radius of the central galaxy.

It is important to highlight that the stellar halos from the GHOSTS survey, Auriga simulations, and L-Galaxies model correspond to spiral galaxies, in most cases MW mass-size ones. These galaxies might exhibit different formation histories leading, for example, to differences in the strength of spiral arms and the presence or absence of stellar bars (see, e.g., [Fragkoudi et al. \(2025\)](#)). However, our sample includes a broader morphological diversity, including elliptical, spiral, and some barred galaxies. Moreover, we did not restrict our selection to MW mass-size galaxies (see Section 2.2). This broader diversity in masses and sizes of the CIELO galaxies can explain the lower metallicities at 30 kpc found in the low-mass stellar halos compared to the GHOSTS galaxies. For these stellar halos, with $\log_{10} M_{\star, \text{halo}} / M_{\odot} < 8.5$, the 30 kpc shell lies further in the outskirts of the galaxy in comparison with r_{vir} . These outer regions are more dominated by metal-poor accreted stars, thereby leading to lower median halo metallicities.

Different apertures to measure the metallicity of stellar halos with the corresponding selection of different stellar populations yield variations in the median metallicity. In the case of the CIELO stellar halos, they have negative metallicity gradients, with the outer region being less metal-poor than the inner one in agreement with previous results ([Bullock & Johnston 2005](#); [Tissera et al. 2014](#)). As mentioned above, we consider the stellar halo region between $1.5r_{\text{opt}}$ to r_{vir} (orange squares in Fig. 1) including all stellar halo populations (in-situ, ex-situ and endo-debris stars) contained in it. This definition extends to inner regions that contain more metal-rich stars and might include in-situ stars, increasing the metallicity with respect to the fixed aperture at 30 kpc (blue squares) about $0.05^{0.30}_{0.01}$ dex (median value, 25th/75th percentiles as subscript/superscript, respectively), as shown in Fig. 1. This aperture adapts to the different masses and sizes of our sample from $z = 0$ to $z \approx 3.5$ and allows us to study the physical processes involved in the assembly of stellar halos. In the future, if other observational apertures are available, we could explore them to make detailed comparisons. We highlight that even using the two different apertures, the 30 kpc or the region between $1.5r_{\text{opt}}$ and r_{vir} , stellar halos follow a mass-metallicity relation.

In [GJ25](#), we showed that outer stellar halos in CIELO galaxies at $z = 0$ are populated mainly by accreted stars, i.e., ex-situ and endo-debris stars ($\sim 80\%$, in a median value), which sets the metallicity of the halo at $z = 0$. In-situ stars shift the median halo metallicity within a standard deviation of $\sigma = \pm 0.03$ dex. With the exception of three galaxies (P7-7805, LG1-2208, and P4-0000) that have in-situ mass fractions ranging from 25 to 40% at $z = 0$, in which cases the in-situ stars increases the median accreted metallicity ~ 0.03 dex up to 0.14 dex. In this work, we study the outer halo including all stellar halo populations (in-situ, ex-situ, and endo-debris stars) contained in it.

In summary, CIELO stellar halos follow the observed MZHR at $z = 0$ (Fig. 1) considering only the accreted component (blue squares, $[\text{Fe}/\text{H}]_{30\text{kpc}} = 0.5 \times \log_{10} M_{\star, \text{halo}} - 5.5$) or the whole halo between $1.5r_{\text{opt}}$ and r_{vir} (orange squares, $[\text{Fe}/\text{H}]_{1.5r_{\text{opt}}-r_{\text{vir}}} = 0.24 \times \log_{10} M_{\star, \text{halo}} - 3.31$). We estimated bootstrap errors for both slopes of 0.1 dex using a 5000 resampling. The simulated MZHR for the outer halos, which includes in-situ, endo-debris and ex-situ stars, has a standard deviation of 0.19 dex. In the following sections, we explore whether the MZHR of the outer halos evolves with time.

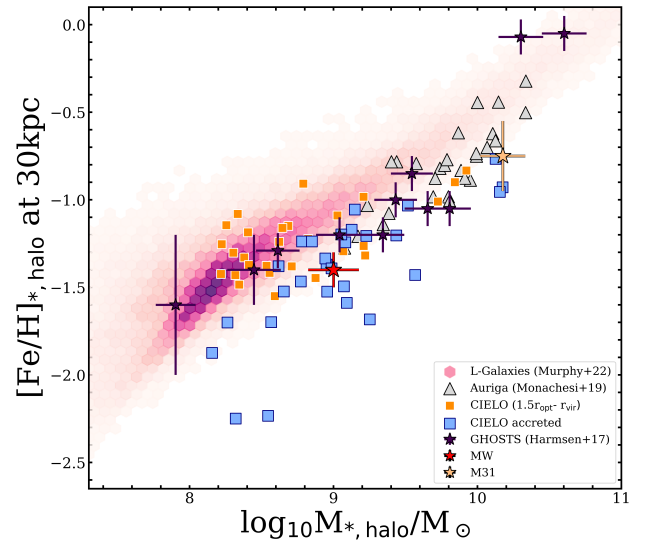


Fig. 1. The mass-metallicity relationship for stellar halos at $z = 0$. Observational data from GHOSTS HST survey ([Harmsen et al. 2017](#); [Gozman et al. 2023](#)) are represented by stars. Estimates for the accreted stellar halo mass and metallicity measured at 30 kpc are displayed for the Auriga galaxies (gray triangles from [Monachesi et al. 2019](#)), the semi-analytic L-Galaxies (pink hexbin from [Murphy et al. 2022](#)) and the CIELO galaxies (blue squares). In addition, we show the CIELO stellar halos measured between $1.5r_{\text{opt}}$ and r_{vir} (orange squares), an aperture that encompasses all stellar populations (in-situ, endo-debris and ex-situ stars).

4. Stellar halo mass metallicity from $z = 3.5$ to $z = 0$

In this section, we investigate the stellar halo mass and metallicity over time. We address the following questions: Is the MZHR already in place at high redshift? If so, does it evolve with time? And how does this evolution proceed? We emphasize that the mass and metallicity are estimated at each redshift following the procedure described in Sec. 2.1, within the radial range from $1.5r_{\text{opt}}$ to r_{vir} . This region includes all the stellar halo populations (i.e., in-situ, endo-debris, and ex-situ stars).

Figure 2 displays a well-defined relation between the stellar halo mass and metallicity from $z = 3.5$ to $z = 0.0$ for the analyzed simulated halos and their progenitors. The rightmost panel shows the full sample of 28 stellar halos at $z = 0$ (also shown in Fig. 1 (orange squares)). As we move to higher redshift, because of our numerical resolution criterion, some halos are not longer included in the analyzed sample. For example, the leftmost panel includes only 16 halos at $z = 3.5$ (see Sec. 2.2). Each panel shows the CIELO MZHR at $z = 0$ (black line), with a shaded gray region indicating its standard deviation ($\sigma = 0.19$ dex). The bottom panel presents the change in metallicity at a given z relative to the present-day value, defined as $\Delta[\text{Fe}/\text{H}] = [\text{Fe}/\text{H}]_z - [\text{Fe}/\text{H}]_{z=0}$. Positive Δ values can arise when galaxies undergo major mergers because the virial and optical radii may be affected and depending on the relaxation timescale of the event, they required some time to reach again dynamical equilibrium, introducing perturbations in the estimations of stellar halo mass and metallicity due to the redistribution of stars from the inner to the outer halo with respect to the $z = 0$ values. It might also be caused by the system moving from the outer to the inner halo, which is not analyzed in this work. In summary, the dispersion at each time is set by the evolutionary track of each stellar halos.

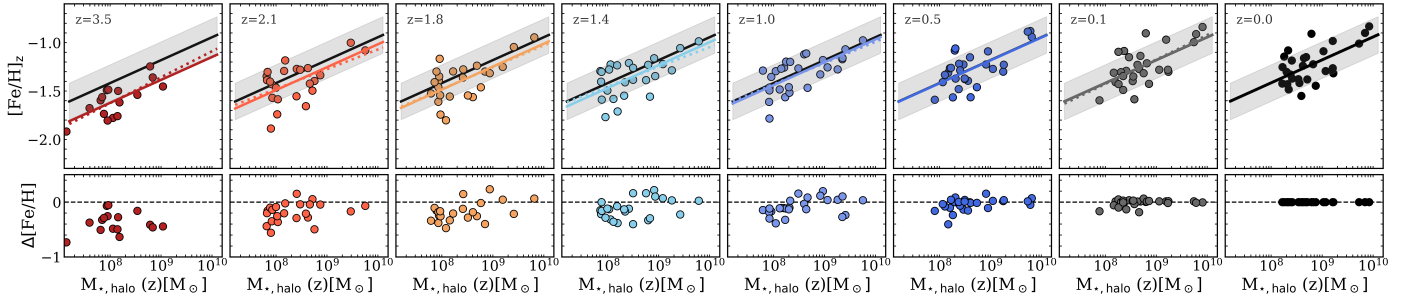


Fig. 2. Top panels: Stellar halo mass and metallicity at different redshifts (indicated in each panel). The black line and gray region show the MZHR at $z = 0$ and its 1σ dispersion. The solid colored lines represent a fit with fixed slope from $z = 0$, minimizing the y-intercept at that redshift. The dashed colored line is a linear fit at each time. Bottom panels: Difference in metallicity with respect to $z = 0$, $\Delta[\text{Fe}/\text{H}] = [\text{Fe}/\text{H}]_z - [\text{Fe}/\text{H}]_{z=0}$, as a function of the stellar halo mass at the same redshift, $M_{\star,\text{halo}}(z)$. Negative Δ values indicate lower metallicities relative to the final values at $z = 0$. Only stellar halos with more than 500 stellar particles are displayed according to our numerical resolution criteria.

The lower panel of Fig. 2 shows that $\Delta[\text{Fe}/\text{H}]$ decreases towards $z = 0$, indicating that stellar halos become progressively enriched, as expected. Low-mass stellar halos primarily accrete material from low-mass galaxies with low star-formation rates (see for example figure 8 and figure 12 from GJ25) and weak gravitational potential wells, which are less prompt to retain metals (Miranda et al. 2025). As a consequence, they contribute with low metallicity stellar population compared to the more massive satellites accreted by high-mass stellar halos, in agreement with previous works (e.g. Gómez & Helmi 2010; D’Souza & Bell 2018b; Fattahi et al. 2020). Hence, we find that the assembly of stellar halos establishes a well-defined MZHR by at least $z \approx 3.5$. We cannot go beyond this redshift because we do not have enough well-resolved stellar halos to make a reliable estimation of the MZHR.

Our simulation predicts only a weak evolution of the MZHR from $z = 3.5$ to $z = 0.0$, indicating that stellar halos become progressively more enriched over time. To quantify this evolution, we explored two approaches: by performing, at each redshift, a linear fit with both slope and intercept treated as free parameters (dotted line in Fig. 2), and by fixing the slope to that of the $z = 0$ MZHR and determining, at each redshift, the intercept that minimizes the residuals (solid line in Fig. 2). Both approaches yield consistent results, with differences in the RMS below 1% at any analyzed redshift. Adopting the fixed-slope method, the MZHR evolves in parallel to MZHR at $z = 0$. Hence, the halo metallicity increases by ≈ 0.21 dex between $z \approx 3.5$ and 0.0 , reflecting a gradual enrichment of stellar halos.

For illustration purposes, Figure 3 displays the evolutionary tracks for four stellar halos in the mass-metallicity plane color-coded by lookback time. The left column shows a high-mass stellar halo ($M_{\star,\text{halo}} = 5.3 \times 10^9 M_\odot$) at the top and a low-mass halo ($M_{\star,\text{halo}} = 2.1 \times 10^8 M_\odot$) at the bottom, while the right column presents two stellar halos with similar masses ($M_{\star,\text{halo}} = 1.6 \times 10^9 M_\odot$). The black line and shaded gray region correspond to the MZHR at $z = 0$ and its standard deviation, respectively. As can be seen from this figure, each stellar halo, regardless of their mass, traces a unique evolutionary path in the mass-metallicity plane. The stellar mass is important to determine the global metallicity of stellar halos (left panels of Fig. 3) but other factors can produce differences in the metallicity at a fixed stellar halo mass (right panels of Fig. 3). For example, mass and the infall and disruption times of the contributing satellites regulate the chemical enrichment of the halo (see also Tau et al. 2025b). In the next section, we further investigate the evolutionary tracks of the stellar halos in a more statistical way and in relation to their assembly histories.

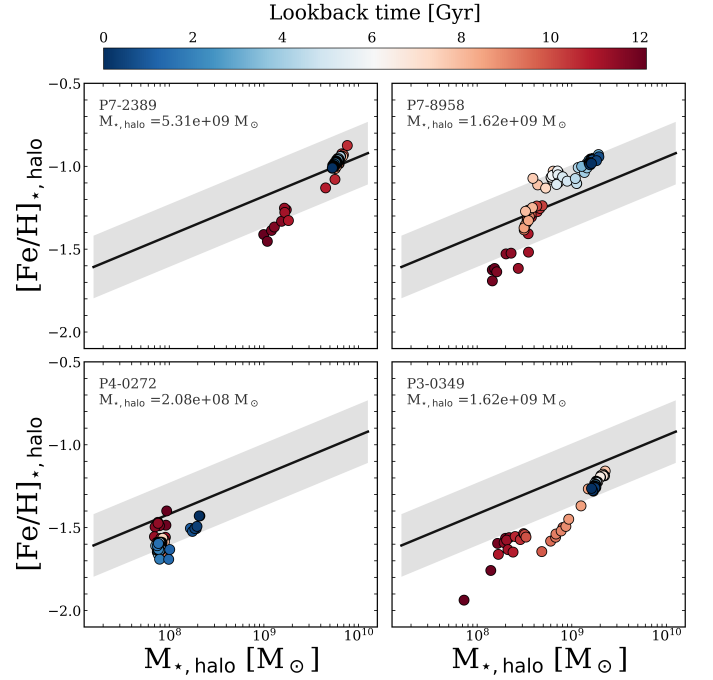


Fig. 3. Stellar halo mass and metallicity of four representative galaxies, color-coded by lookback time. The CIELO MZHR at $z = 0$ and 1σ dispersion are shown as a black and shaded gray region, respectively. CIELO galaxy ID and stellar halo mass are displayed in the upper-right corner of each panel.

5. The heartbeat of stellar halos

In this section, we adopt an analogy inspired by the medical field, drawing a parallel between electrocardiograms and the assembly of stellar halos. In cardiology, electrocardiograms record the electrical activity of the heart (Krikler 1987) and reveal irregularities in cardiac rhythm (Fye 1994) or the absence of heartbeats when the signal flattens. Similarly, we present cardiograms that describe the assembly of stellar halos, with the heartbeats represented by variations in their median metallicity and stellar mass. A flat line indicates a quiescent or stable time, where the median metallicity or stellar halo mass do not change significantly within a threshold of ± 0.1 dex⁴ of its value at $z = 0$.

⁴ This threshold falls within the standard deviation of the MZHR at $z = 0$ ($\sigma = 0.19$ dex). Slight variations do not affect our results.

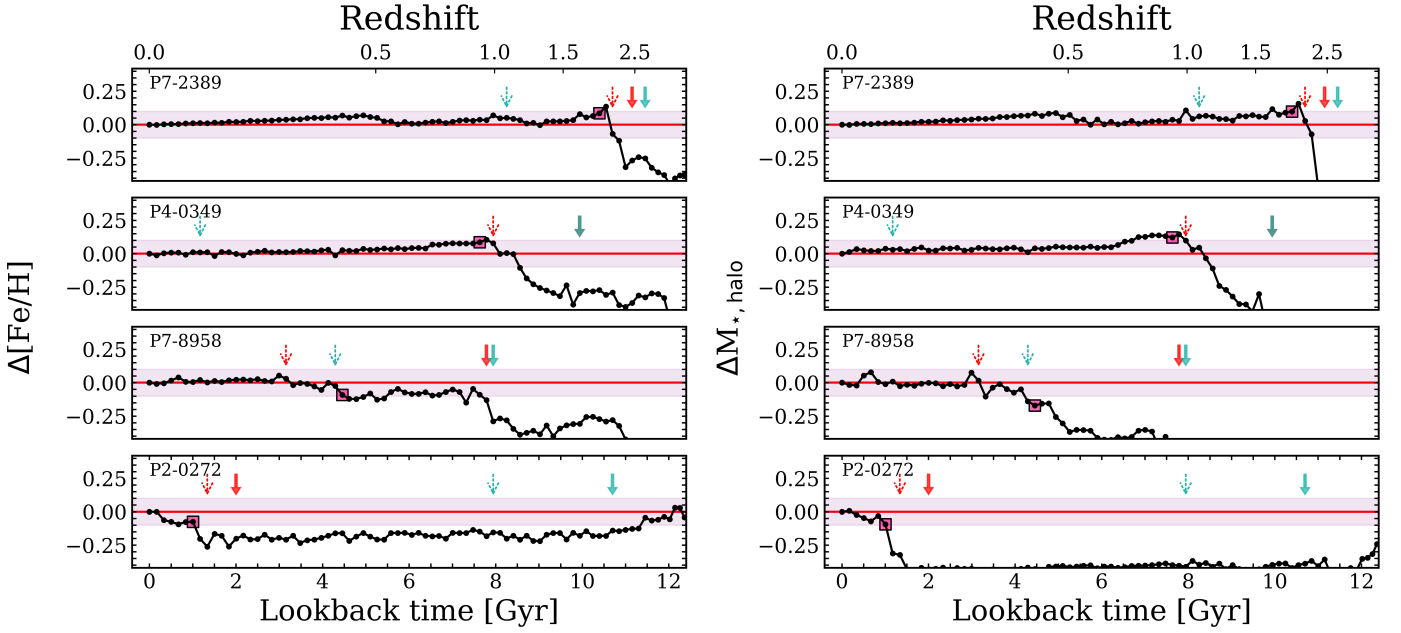


Fig. 4. Variations in metallicity (left column) and stellar halo mass (right column) relative to their values at $z = 0$ as a function of lookback time. The arrows indicate the main stellar contributors: SHMC1 (red) and SHMC2 (light blue) at infall (solid) and merger (dotted) times. The pink shaded region marks differences within ± 0.1 dex from $z = 0$ of the stellar mass or metallicity. The pink square represent the stability time defined in Sec. 5.

To illustrate this new approach, Figure 4 presents the cardiograms for the same four stellar halos shown in Fig. 3. The cardiograms for the remaining 23 stellar halos⁵ are displayed in the Appendix A. The left column shows variations in the median stellar halo metallicity, $\Delta[\text{Fe}/\text{H}]$ as defined in the previous section.

The right column displays changes in the stellar halo mass, defined as $\Delta M_{*,\text{halo}} = \log_{10}(M_{*,\text{halo}}(z)) - \log_{10}(M_{*,\text{halo}}(z=0))$, as a function of the lookback time. Negative values of $\Delta[\text{Fe}/\text{H}]$ or $\Delta M_{*,\text{halo}}$ indicate that at the corresponding lookback time, the stellar halo is more metal-poor (left panel) or less massive (right panel) than at its final state at $z = 0$. The pink shaded region marks the epochs when the mass or metallicity is within ± 0.1 dex of its final value at $z = 0$. The arrows denote the infall time (solid) and the merger time (dotted) of SHMC1 (red) and SHMC2 (light blue).

The growth of stellar mass and metallicity follows broadly similar trends with time, reflecting their connection through star formation, stellar evolution, and galaxy assembly. Variations in metallicity and mass are shown since $z \approx 3.5$ moving towards $z = 0$ (decreasing lookback time). As shown in this figure, galaxies approach a metallicity plateau at a given epoch. We define the stability time (t_{stable}) as the first lookback time, traced backward from $z = 0$, when the median halo metallicity reaches a value within ± 0.1 dex respect to its value at $z = 0$ (pink shades). This time is indicated by a pink square in Fig. 4.

The stability time is defined from the metallicity cardiogram because even when the halo reaches this quiescent phase in global metallicity, it does not imply a complete cessation of satellite accretion, and hence, of the growth in mass. In fact, the stellar halo mass at t_{stable} , accounts for 56₄₇⁶³% of its value at $z = 0$ (median; lower and upper indices denote the 25th-75th percentiles, respectively). A further 12₉²⁰% of stars were in the inner

halo or host galaxy at t_{stable} . Some stars can temporally populate the inner halo or galaxy at t_{stable} , because they belong to a satellite undergoing disruption at t_{stable} , which is no longer identified by the SUBFIND algorithm, resulting in debris deposited in the outer halo at $z = 0$. While other stars are dynamically heated by mergers or interactions, ending up in the stellar halo by $z = 0$. A small fraction (0.39_{0.03}^{3.77}%) of stars were born after t_{stable} and ended up in the stellar halo at $z = 0$. Finally, 25₁₂³⁶% of halo stars at $z = 0$ are accreted later than t_{stable} . However, their metallicity exhibits a median deviation of only ~ -0.02 dex from the $z = 0$ value. Therefore, this additional stellar mass does not significantly alter the median metallicity established at t_{stable} .

The increase in metallicity in the stellar haloes is primarily driven by the accretion of dwarf galaxies, which follow a MZ_★R (see Muñoz-Escobar et al. (2025), for a discussion of the MZR of disrupted satellites in CIELO simulations). Satellites can experience ongoing star formation after infalling (Tissera et al. 2014; Slater & Bell 2014; Geha et al. 2017). These stars represent an important formation channel in stellar halos, accounting for $\sim 30\%$ of the accreted halo mass at $z = 0$, and are slightly more metal-rich and younger than the ex-situ stars, further enhancing the overall halo metallicity (GJ25). Hence, the progressive contribution of the satellite galaxies leads to a systematic enrichment of the stellar halo over time, as shown in Fig. 2 and Fig. 3.

Figure 5 compiles all halo cardiograms by shifting the time to $t - t_{\text{merger}}^{\text{SHMC1}}$, where $t_{\text{merger}}^{\text{SHMC1}}$ is the merger time of SHMC1 that ranges from 0.5 to 11 Gyr depending on the assembly path of each stellar halo. Before SHMC1 is fully disrupted, ΔM and $\Delta[\text{Fe}/\text{H}]$ show substantial scatter with median values of $-0.41_{-0.54}^{+0.19}$ and $-0.17_{-0.29}^{+0.07}$ dex, respectively. After $t_{\text{merger}}^{\text{SHMC1}}$, the scatter drops significantly to $0.002_{-0.03}^{+0.04}$ and $0.01_{-0.004}^{+0.03}$ dex, respectively. Therefore, the main contributing satellite plays a key role in setting the stability time, from which the metallicity of stellar halos cease to increase significantly. This agrees with previous works, supporting the idea that the main contributor of the stellar halo is determining MZ_★R at $z = 0$ (Harmsen et al.

⁵ For the following results, we analyzed 27 stellar halos because one galaxy, LG1-4469, has a surviving SHMC1, therefore it was not considered because we can not estimate a disruption time for their SHMC1.

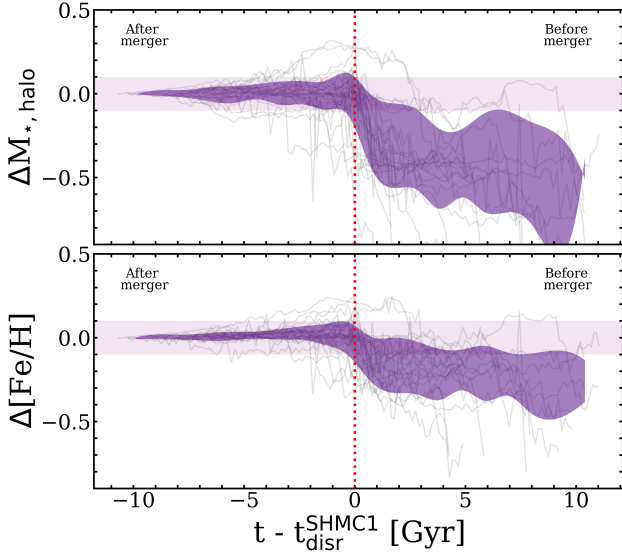


Fig. 5. Variations in stellar halo mass (upper panel) and metallicity (lower panel) as a function of lookback time, offset by the merger time of their SHMC1. The purple shaded region represents ± 1 standard deviation (16th and 84th percentiles) of the total sample. The pink shaded region indicates a ± 0.1 dex variation in mass (upper panel) or metallicity (lower panel) relative to $z = 0$.

2017; D’Souza & Bell 2018b; Monachesi et al. 2019). The stability time serves as a proxy for the moment when a stellar halo reaches the present-day MZhr, within the standard deviation.

Figure 6 shows a strong correlation between t_{stable} and $t_{\text{SHMC1 merger}}^{\text{SHMC1}}$ (Spearman coefficient $r = 0.72$ and $p\text{-value} < 2e - 05$) with a scatter of $\sigma = 2.2$. The color scale quantifies the importance of SHMC1 respect to the second and third main contributor, i.e. $\Delta f_{\text{dom}} = f_{\text{mass}}^{\text{SHMC1}} - f_{\text{mass}}^{\text{SHMC2+SHMC3}}$. Higher values of Δf_{dom} correspond to halos dominated by a single massive accretion event.

Stellar halos near the one-to-one line tend to assemble most of its stellar mass by the accretion of the SHMC1. They typically reach chemical stability when the disruption of SHMC1 is completed⁶, suggesting that this marks the end of significant enrichment, as shown by the drop in $\Delta[\text{Fe}/\text{H}]$ in the halo cardiograms (see Fig. 5). Stellar halos above the one-to-one relation reach t_{stable} before SHMC1 has completely merged, indicating that other contributors set the level of enrichment of the halo at early time. In these cases, we find that SHMC2 and SHMC3 together are the ones responsible of this. For halos below the one-to-one line, the contributions of SHMC2 and SHMC3 are also relevant but they contributed at a more recent time in comparison to SHMC1.

In summary, for high Δf_{dom} , the stellar halo is mainly assembled through a single dominant accretion event that sets its overall metallicity, contributed by more than 40 percent on average, in agreement with D’Souza & Bell (2018b). In such cases, t_{stable} closely matches $t_{\text{SHMC1 merger}}^{\text{SHMC1}}$, making t_{stable} a useful proxy for constraining the merger time of the last major accretion event that builds up the stellar halo. We recall that merger time is defined as the epoch when the satellites is fully disrupted. In contrast, when Δf_{dom} is small or negative, SHMC2 and SHMC3 contribute

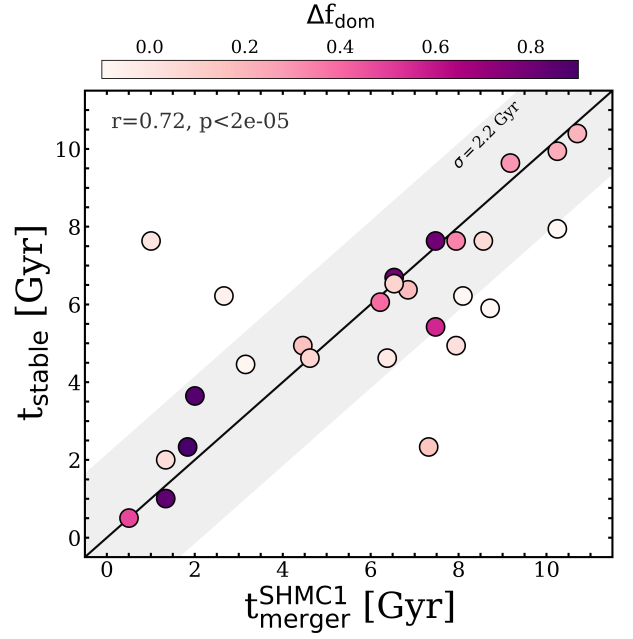


Fig. 6. The stability time (t_{stable}) as a function of the merger time of the SHMC1 ($t_{\text{SHMC1 merger}}^{\text{SHMC1}}$), color-coded by the difference between the mass fraction of the SHMC1 and the combined contribution from the SHMC2 and SHMC3 (i.e. $\Delta f_{\text{dom}} = f_{\text{mass}}^{\text{SHMC1}} - f_{\text{mass}}^{\text{SHMC2+SHMC3}}$). The black line is 1:1 line and the gray area is the standard deviation of the residual between t_{stable} and $t_{\text{SHMC1 merger}}^{\text{SHMC1}}$.

more substantially to the metallicity of the stellar halo, driving the scatter ($\sigma = 2.2$ Gyr) in the $t_{\text{stable}} - t_{\text{SHMC1 merger}}^{\text{SHMC1}}$ plane. Depending on the location on the $t_{\text{stable}} - t_{\text{SHMC1 merger}}^{\text{SHMC1}}$ plane the relative time when the contributions occurred could be deduced. Therefore, we suggest that the $t_{\text{stable}} - t_{\text{SHMC1 merger}}^{\text{SHMC1}}$ plane stores information on the importance and the chronology of the multiple SHMCs to the formation of the stellar halos.

6. Observational Implications

Our findings suggest that an estimation of the stability time provides a proxy of the merger time of the main contributing satellite that build up the stellar halo of galaxies, and combined with an estimation of $t_{\text{SHMC1 merger}}^{\text{SHMC1}}$ could provide clues about the relative importance of the second and third main progenitors. We explore possible observational proxies to infer the t_{stable} .

Recent observational advances have made it possible to estimate the stellar halo age of nearby galaxies using GHOSTS data. Harmsen et al. (2023) used the AGB/RGB ratio to constrain t_{90} , defined as the time before which 90 percent of the halo stars were formed. In order to mimic this observational estimation, we computed t_{90} from the cumulative stellar mass as a function of age of the stars belonging to the simulated stellar halo at $z = 0$. Additionally, we built the halo cardiogram using the age-metallicity relationship (AMR) of the simulated halo stars at $z = 0$. In this way, we also estimate a proxy for the stability time (t_{AMR}) from the age-metallicity relation, defined as the age of the populations at which their cumulative metallicity reach a value 0.1 dex of the overall halo metallicity at $z = 0$. In what follows, we explore the relation between t_{stable} and both t_{90} and t_{AMR} .

Figure 7 shows the correlation between t_{stable} and t_{90} (purple circles, $r = 0.64$ and $p < 4e - 04$), and t_{AMR} (pink circles, $r = 0.55$ and $p < 3e - 03$). Both relations can be fitted by linear regressions,

⁶ We note that if a satellite is assumed to be part of the stellar halo as soon as it gets into the virial radius of the halo, then time of infall should be considered as a reference time. In this work we follow the satellite as a separate structure until it can be longer identified. Hence the contribution of stars to the stellar halo is followed as the satellite is disrupted.

Table 1. Observed properties of nearby galaxies available in the literature and t_{stable} estimated from this article.

Galaxy	$M_{\star, \text{gal}}$ [$10^{10} M_{\odot}$]	t_{90} [Gyr]	$t_{\text{stable}}(M_{\star, \text{gal}})$ [Gyr]	$t_{\text{stable}}(t_{90})$ [Gyr]	References $M_{\star, \text{gal}}, t_{90}$
NGC 253	5.5 ± 1.4	6.2 ± 1.5	7.8	5.0	H17, H23
NGC 891	5.3 ± 1.3	6.9 ± 1.6	7.8	5.6	H17, H23
NGC 3031	5.6 ± 1.4	11.8 ± 4.0	9	9.9	H23, H23
NGC 5128	20	2.5 ± 0.5	9.1	1.7	F&R18, H17
NGC 4565	8.0 ± 2.0		8.2		H17
NGC 4945	3.8 ± 0.95		7.4		H17
NGC 7814	4.5 ± 1.1		7.6		H17
M31	10.3 ± 2.3	2.5 ± 0.5	8.4	1.7	L&N15, H23
MW	6.1 ± 1.1	10	7.9	7.5	S15, H23

Notes. From left to right: Galaxy, name of the observed galaxy; $M_{\star, \text{gal}}$, observed stellar galaxy mass; t_{90} , observational time at which 90 per cent of the stars are formed; t_{stable} lookback time estimated from the linear regression with galaxy stellar mass (see Sec. 6); t_{stable} lookback time inferred from the correlation with t_{90} following eq. 1a. References from which the $M_{\star, \text{gal}}$ and t_{90} were obtained, H17: Harmsen et al. (2017), H23: Harmsen et al. (2023), F&R18: Fall & Romanowsky (2018), L&N15: Licquia & Newman (2015), S15: Sick et al. (2015)

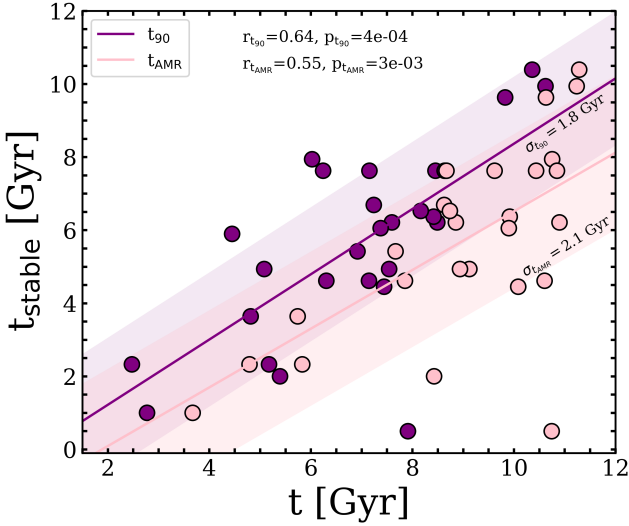


Fig. 7. The stability time, t_{stable} , as function of the time: t_{90} (purple) defined as the time at which 90 percent of the stars formed and t_{AMR} (pink) defined as an observed stability time from the age-metallicity at $z = 0$. Colored lines are linear fits and shaded regions denote the standard deviation of the data. Spearman and p-value coefficient are display at the top center.

$$t_{\text{stable}} = 0.89 t_{90} - 0.56 \quad (1a)$$

$$t_{\text{stable}} = 0.80 t_{\text{AMR}} - 1.51 \quad (1b)$$

The scatter is quantified by the standard deviation of $\sigma = 1.8$ and 2.1 Gyr for $t_{\text{stable}} - t_{90}$ and $t_{\text{stable}} - t_{\text{AMR}}$, respectively. These results suggest that the epoch at which the stellar halo metallicity stabilizes is closely linked to the time by which most of the halo stars were formed, t_{90} . In this sense, the stability time can be interpreted as a chemical proxy for the halo formation time. It is important to note that halo stars mostly form in dwarf galaxies at early epochs and are accreted into the host galaxy at later times. For this reason, we emphasize the distinction between t_{90} and the time at which those stars were actually accreted into the stellar halo.

Hence, we use t_{90} measurements from GHOSTS data (Harmsen et al. 2023) and our predicted relation given by equation 1a to estimate t_{stable} . These predictions are displayed in Table 1 and the implications are discussed in the next Section. We do not report estimations of t_{AMR} for these galaxies because there are not resolved stellar populations available. An estimation could be attempted for the MW but it implies a major observational work which is beyond the scope of this paper.

Finally, another relevant observable is the stellar mass of galaxies. We find a trend between the galaxy stellar mass and t_{stable} , where more massive galaxies tend to stabilize their metallicity at earlier times than low-mass galaxies, consistent with a downsizing scenario. The relation is displayed in Figure 8. The scatter ($\sigma = 2.6$ Gyr) is significant as expected on the basis of the previous discussion where we show that each halo has its own evolutionary track even more for similar masses (Fig. 3). However, the correlation is clear with $r = 0.39$ ($p = 0.05$). A linear regression fit yields $t_{\text{stable}} = 2.25 \times \log_{10} M_{\star, \text{gal}} - 16.33$.

7. Discussion

Our results reveal a correlation between $t_{\text{merger}}^{\text{SHMC1}}$ and t_{stable} that follows a one-to-one relation, with a scatter of 2.2 Gyr (Fig. 6). This correlation arises because SHMC1 is typically more massive, and following the MZ \star R, more metal-rich than other contributing satellites, which tend to be less massive (see also Muñoz-Escobar et al. 2025). Consequently, for halos in the one-to-one line in the $t_{\text{stable}} - t_{\text{merger}}^{\text{SHMC1}}$, the debris of SHMC1 sets the halo metallicity at t_{stable} , and later accretions do not significantly alter the median metallicity established at t_{stable} . This is consistent with the results of Harmsen et al. (2017), who suggest that the main contributor sets the metallicity of the halo, and the following numerical works by D’Souza & Bell (2018b) and Monachesi et al. (2019). Halos with larger residuals in the $t_{\text{merger}}^{\text{SHMC1}} - t_{\text{stable}}$ plane, have SHMC2 and SHMC3 that together contribute with comparable or higher mass fractions than SHMC1 (i.e. smaller Δf_{dom}), implying that the median halo metallicity is not set by the SHMC1, and other satellite contributors are needed. This occurs because, although the stellar mass of the satellite is important in determining its metallicity, the mass contributed by the satellite to the stellar halo also depends on its orbital parameters,

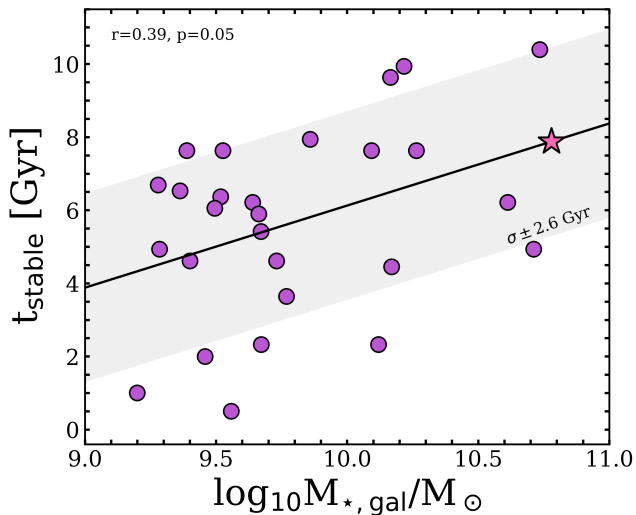


Fig. 8. Stability time, t_{stable} , as a function of stellar galaxy mass, $M_{\star,\text{gal}}$. The black line corresponds to a linear regression shown in eq. 1a, and the gray shaded region denotes the standard deviation of t_{stable} . The Milky Way is included as a reference, adopting $M_{\star,\text{gal}} = 6.08 \pm 1.14 \times 10^{10} M_{\odot}$ from (Sick et al. 2015) (pink star).

which will influence how the material is distributed in the halo and galaxy. Furthermore, whether the satellite is fully disrupted or survives longer in the halo, or if it is gas-rich or gas-poor also influence their metallicity and the metal content that contributed to the halo, since they could sustain star formation longer, increasing their metallicity.

By using our predicted relations (eq. 1a), we estimate that the last major merger of the MW took place at ~ 7.5 Gyr, consistent, within uncertainties, with the $\sim 8 - 11$ Gyr window associated with Gaia Enceladus Sausage (GES) (Helmi et al. 2018; Belokurov et al. 2018; Di Matteo et al. 2019; Gallart et al. 2019; Giribaldi & Smiljanic 2023). If GES is the last major accretion event of the MW that built up the bulk of the stellar halo, its debris would drive the present stellar halo metallicity. However, if other accretion events such as Sagittarius, contribute significantly to the halo assembly, the merger time obtained from our predictions would be slightly underestimated.

Table 1 also provides predictions for NGC 3031 (M81). This galaxy is in an early stage interaction with M82 and NGC 3077 (Smercina et al. 2020). Harmsen et al. (2023) derived $t_{90} = 11.8 \pm 4$, noting that the AGB/RGB ratio is poorly measured, which makes this estimation of t_{90} uncertain. An independent constraint comes from Durrell et al. (2010) who report a mean age⁷ of 9 ± 2 Gyr for the dominant halo population of a field at a projected distance of 19 kpc from the center of M81. Using that mean age in our predicted relation (eq. 1a), we infer $t_{\text{stable}} = 7.81$ Gyr, which is ~ 2 Gyr younger than the $t_{\text{stable}} \approx 10$ Gyr inferred from the t_{90} measurement of Harmsen et al. (2023). If the stellar halo of M81 is dominated by debris of a single merger, we predict that this event happened in the early stage of M81. However, because of the large merger rate (1:2) estimated for the ongoing interaction with M82, we expect that the stellar halo of M81 might be temporarily displaced from the MZHR until the major accretion event ceases. An approach to es-

timate the scatter in the $t_{\text{stable}} - t_{\text{merger}}^{\text{SHMC1}}$ plane would be to estimate the relative contribution coming from M82.

For Andromeda galaxy, M31, the $M_{\star,\text{gal}} - t_{\text{stable}}$ and $t_{90} - t_{\text{stable}}$ relations yield markedly different merger times (assuming $t_{\text{stable}} \approx t_{\text{merger}}^{\text{SHMC1}}$). From $M_{\star,\text{gal}} - t_{\text{stable}}$ relation, we infer the last major merger took place about 8.4 Gyr ago. In contrast, the $t_{90} - t_{\text{stable}}$ relation gives an estimation of the merger time of 1.7 Gyr ago. The latter one agrees with evidence of an active recent merger history suggested by a $\sim 2 - 3$ Gyr burst of star formation that can be explained by a recent major merger event that triggered it (Hammer et al. 2018; D’Souza & Bell 2018a; Escala et al. 2020; Tsakonas et al. 2025). This suggests that M31 just reached MZHR at $z = 0$ consistent with the observational data shown in Fig. 3. Moreover, if its last major merger contributed with high Δf_{dom} , its metallicity would be driven by that event, which we predict happened at about 1.7 Gyr ago.

Even though M31 and MW have comparable stellar galaxy masses, they show different accretion histories which lead to different stability times as well as distinct stellar halo masses and metallicities. Hence they are expected to trace different evolutionary paths as shown in the left column in Fig. 3.

Finally, the stability time inferred from the galaxy stellar mass relation should be interpreted with caution due to the diversity in formation histories of galaxies, reflected in the variety of halo mass fractions at a fixed $M_{\star,\text{gal}}$, as was discussed for M31 and MW. The large scatter ($\sigma = 2.6$ Gyr) in the $M_{\star,\text{gal}} - t_{\text{stable}}$ plane might reflect the stochastic nature of galaxy formation and limits the precision of t_{stable} inferred from $M_{\star,\text{gal}}$ alone. Larger samples are needed to test this trend and probe any secondary dependence.

A numerical caveat to our result is the uncertainty in defining the moment when stellar material from a dwarf galaxy becomes part of the main halo (referred to as merger time in this work). This timing likely depends on several factors, including the sub-halo identification algorithm and the merger tree construction method. Observationally, identifying this transition is equally challenging, as it is not always clear when a tidally stripped dwarf galaxy should no longer be classified as a distinct system (e.g., the case of the Sagittarius dwarf in the Milky Way). Additionally, stellar halos are expected to have in-situ stars, which might have different origin. GJ25 showed that for these halos the fraction of in-situ is about 20%. However, we note that in our estimations, we have considered them to calculate t_{90} and hence, the simulated relation between t_{stable} and t_{90} already considered the possible presence of in-situ stars at higher galactocentric distances.

8. Summary and conclusions

We used CIELO zoom-in simulations (Tissera et al. 2025) to investigate the stellar MhZR of galaxies with stellar masses in the range of $\log_{10}(M_{\star,\text{gal}}/M_{\odot}) \in [9, 11]$. Stellar halos were isolated using the AM-E method (Tissera et al. 2012) following the procedure in GJ25. We identified the stellar halo between $1.5r_{\text{opt}}$ and r_{vir} , from $z \approx 3.5$ to $z = 0$, to evaluate the existence of the MZHR at high redshift and characterize whether it evolves with time.

The CIELO galaxies reproduce the MZHR at $z = 0$, in agreement with previous observational and theoretical studies (D’Souza & Bell 2018b; Monachesi et al. 2019; Smercina et al. 2022; Tau et al. 2025a). This correlation holds whether we consider only the accreted component or the whole stellar halo populations within $1.5r_{\text{opt}}$ to r_{vir} (Fig 1). The calculated slope for CIELO halos at 30 kpc, $m = 0.5 \pm 0.1$, is slightly shallower than that reported by Harmsen et al. (2017), $m = 0.7 \pm 0.2$, albeit

⁷ Using deep color-magnitude diagram from the Hubble Space Telescope, they obtained the mean age from the shape of the red giant branch, the magnitude of the red clump, and the location of the red giant branch bump.

within one sigma, while it is consistent with that reported by [Murphy et al. \(2022\)](#), $m = 0.51$. We note that our sample spans a broader range of galaxy morphologies and masses, whereas previous studies focused primarily on Milky Way mass-like galaxies.

We find a well-defined MZhr from $z \approx 3.5$ to $z = 0$, described by linear fits, that slightly evolves while preserving the slope at $z = 0$ (Fig. 4). For reference, a stellar halo with $M_{\star, \text{halo}} = 10^9 M_{\odot}$ increases its metallicity by ~ 0.21 dex from $z \approx 3.5$ to $z = 0$. These results are consistent with a progressive accretion of dwarf galaxies, which follow a mass-metallicity relation, driving the systematic enrichment shown in the stellar halos over time.

To characterize when halos settle on the present-day MZhr, we define the halo cardiograms (median halo metallicity relative to their values at $z = 0$ as a function of time, Fig. 4) to identify the lookback time (t_{stable}) at which the median stellar halo metallicity remains within ± 0.1 dex of its value at $z = 0$. We find that t_{stable} and the merger time of the first stellar halo main contributor (SHMC1) follows a one-to-one relation, with a scatter of ~ 2 Gyr (Fig. 6). When the mass fraction of SHMC1 is higher than the remaining contributors by at least 20%, the stellar halo metallicity is stabilized once SHMC1 is fully disrupted. In this case, the stability time can be used as a proxy to estimate the merger time of the main contributing satellite that build up the stellar halo. This relation has a dispersion due to the fact that for some halos, the second and third contributors are significant and could contribute to set distinct evolutionary paths.

We show that an observational cardiogram of the stellar halos can be built from the age-metallicity relation. By applying the same criteria used for the simulated cardiograms, we estimated t_{AMR} , which is found to correlate with t_{stable} . However, this is currently difficult to perform observational due to low surface brightness of stellar halos. Hence, we explore t_{90} as an observational proxy for dating the moment at which a stellar halo reaches the local MZhr and, by using the simulated correlation shown in eq. 1a, estimating the time of the main merger event that contributed to built up it. We find an excellent correlation between t_{stable} and t_{90} , which we use to predict the time of complete disruption of the main contributor of several observed halos including the MW (Table 1). For the MW, our estimate yields ~ 7.5 Gyr with an RMS of 2.2 Gyr, consistent within the uncertainties with the $\sim 8 - 10$ Gyr window associated with GES, although this estimate would be less robust if the Sagittarius merger contributed a larger mass fraction to the MW's stellar halo. If we take 10 Gyr as the reference time for the GES merger and consider it as SHMC1, then our findings suggest that Sagittarius contributes significantly to the build up of the MW's stellar halo. On the other hand, for M31, we predict a recent stability scenario for the MZhr, delayed by a merger event that we predict took place at ~ 1.7 Gyr ago.

Future estimations of the stellar metallicities of galaxies and their stellar halos at low and high redshift will provide crucial data for test our predictions and improve our understanding of galaxy formation.

Acknowledgements. We thank useful comments by Paula Jofré, Claudia Lagos and Rolando Dunner. JGJ acknowledges funding by ANID (Beca Doctorado Nacional, Folio 21210846). JGJ, PBT and AM acknowledge support from the ANID BASAL project FB210003. PBT acknowledges partial funding by Fondecyt-ANID 1240465/2024. AM acknowledges support from the ANID FONDECYT Regular grant 1251882. BTC gratefully acknowledges funding by ANID (Beca Doctorado Nacional, Folio 21232155). SP acknowledge partial support from CONICET through grant PIP 11220210100214. RDT thanks the Ministerio de Ciencia e Innovación (Spain) for financial support under Project grant PID2021-122603NB-C21 as well as Project PID2024-156100NB-C21 fi-

nanced by MICIU/AEI/10.13039/501100011033/FEDER, EU. This work has received funding from the European Union's HORIZON-MSCA-2021-SE-01 Research and Innovation Programme under the Marie Skłodowska-Curie grant agreement number 101086388 - Project acronym:LACEGAL. This project used the Ladgerda Cluster (Fondecyt 1200703/2020 hosted at the Institute for Astrophysics, Chile), the NLHPC (Centro de Modelamiento Matemático, Chile), Geryon clusters (Center for Astrophysics, CATA, Chile), and the Barcelona Supercomputer Center (Spain).

References

- Amorisco, N. C. 2017, *Monthly Notices of the Royal Astronomical Society: Letters*, 469, L48–L52
- Bell, E. F., Monachesi, A., Harmsen, B., et al. 2017, *ApJ*, 837, L8
- Belokurov, V., Erkal, D., Evans, N., Koposov, S., & Deason, A. 2018, *MNRAS*, 478, 611
- Bullock, J. S. & Johnston, K. V. 2005, *ApJ*, 635, 931
- Cañas, R., Lagos, C. d. P., Elahi, P. J., et al. 2020, *MNRAS*, 494, 4314
- Casanueva-Villarreal, C., Tissera, P. B., Padilla, N., et al. 2024, *arXiv e-prints*, arXiv:2405.02206
- Cataldi, P., Pedrosa, S. E., Tissera, P. B., et al. 2023, *MNRAS*, 523, 1919
- Cooper, A. P., Frenk, C. S., Hellwing, W. A., & Bose, S. 2025, *Simulations of the accreted stellar halos of low-mass field galaxies*
- Cooper, A. P., Parry, O. H., Lowing, B., Cole, S., & Frenk, C. 2015, *MNRAS*, 454, 3185
- Davé, R., Rafieferantsoa, M. H., Thompson, R. J., & Hopkins, P. F. 2017, *MNRAS*, 467, 115
- Davis, M., Efstathiou, G., Frenk, C. S., & White, S. D. M. 1985, *ApJ*, 292, 371
- De Rossi, M. E., Theuns, T., Font, A. S., & McCarthy, I. G. 2015, *MNRAS*, 452, 486
- Deason, A. J., Mao, Y.-Y., & Wechsler, R. H. 2016, *ApJ*, 821, 5
- Di Matteo, P., Haywood, M., Lehnert, M. D., et al. 2019, *Astronomy & Astrophysics*, 632, A4
- Dolag, K., Borgani, S., Murante, G., & Springel, V. 2009, *Monthly Notices of the Royal Astronomical Society*, 399, 497–514
- Domínguez-Gómez, J., Pérez, I., Ruiz-Lara, T., et al. 2023, *Astronomy & Astrophysics*, 680, A111
- D'Souza, R. & Bell, E. F. 2018a, *Nature Astronomy*, 2, 737
- D'Souza, R. & Bell, E. F. 2018b, *MNRAS*, 474, 5300
- Durrell, P. R., Sarajedini, A., & Chandar, R. 2010, *The Astrophysical Journal*, 718, 1118–1127
- Elias, L. M., Sales, L. V., Creasey, P., et al. 2018, *Monthly Notices of the Royal Astronomical Society*, 479, 4004–4016
- Escala, I., Gilbert, K. M., Kirby, E. N., et al. 2020, *The Astrophysical Journal*, 889, 177
- Fall, S. M. & Romanowsky, A. J. 2018, *The Astrophysical Journal*, 868, 133
- Fattahi, A., Deason, A. J., Frenk, C. S., et al. 2020, *MNRAS*, 497, 4459
- Font, A. S., Johnston, K. V., Bullock, J. S., & Robertson, B. E. 2006, *ApJ*, 646, 886
- Font, A. S., McCarthy, I. G., Poole-Mckenzie, R., et al. 2020, *MNRAS*, 498, 1765
- Fragkoudi, F., Grand, R., Pakmor, R., et al. 2025, *Bar formation and evolution in the cosmological context: Inputs from the Auriga simulations*
- Freeman, K. & Bland-Hawthorn, J. 2002, *Annual Review of Astronomy and Astrophysics*, 40, 487
- Fye, W. B. 1994, *Am. J. Cardiol.*, 73, 937
- Gallart, C., Bernard, E. J., Brook, C. B., et al. 2019, *Nature Astronomy*, 3, 932
- Gallazzi, A., Charlot, S., Brinchmann, J., White, S. D. M., & Tremonti, C. A. 2005, *Monthly Notices of the Royal Astronomical Society*, 362, 41–58
- Geha, M., Wechsler, R. H., Mao, Y.-Y., et al. 2017, *The Astrophysical Journal*, 847, 4
- Genel, S., Vogelsberger, M., Springel, V., et al. 2014, *Monthly Notices of the Royal Astronomical Society*, 445, 175–200
- Giribaldi, R. E. & Smiljanic, R. 2023, *A&A*, 673, A18
- Gómez, F. A. & Helmi, A. 2010, *MNRAS*, 401, 2285
- Gonzalez-Jara, J., Tissera, Patricia B., Monachesi, Antonela, et al. 2025, *A&A*, 693, A282
- Gozman, K., Bell, E. F., Smercina, A., et al. 2023, *ApJ*, 947, 21
- Grimozzi, S. E., Font, A. S., & De Rossi, M. E. 2024, *MNRAS*, 530, 95
- Hammer, F., Yang, Y. B., Wang, J. L., et al. 2018, *MNRAS*, 475, 2754
- Harmsen, B., Bell, E. F., D'Souza, R., et al. 2023, *Constraining the assembly time of the stellar haloes of nearby Milky Way-mass galaxies through AGB populations*
- Harmsen, B., Monachesi, A., Bell, E. F., et al. 2017, *MNRAS*, 466, 1491
- Helmi, A., Babusiaux, C., Koppelman, H. H., et al. 2018, *Nature*, 563, 85
- Khoperskov, S., Minchev, I., Libeskind, N., et al. 2023, *A&A*, 677, A91
- Kirby, E. N., Cohen, J. G., Guhathakurta, P., et al. 2013, *ApJ*, 779, 102

- Knollmann, S. R. & Knebe, A. 2009, *The Astrophysical Journal Supplement Series*, 182, 608–624
- Krikler, D. M. 1987, *Cardiology Clinics*, 5, 349, 12-Lead Electrocardiography
- Langeroodi, D., Hjorth, J., Chen, W., et al. 2023, *The Astrophysical Journal*, 957, 39
- Lee, H., Skillman, E. D., Cannon, J. M., et al. 2006, *ApJ*, 647, 970
- Lequeux, J., Peimbert, M., Rayo, J. F., Serrano, A., & Torres-Peimbert, S. 1979, *A&A*, 80, 155
- Licquia, T. C. & Newman, J. A. 2015, *ApJ*, 806, 96
- Ma, X., Hopkins, P. F., Faucher-Giguère, C.-A., et al. 2015, *Monthly Notices of the Royal Astronomical Society*, 456, 2140–2156
- Maiolino, R. & Mannucci, F. 2019, *The Astronomy and Astrophysics Review*, 27
- Maiolino, R., Nagao, T., Grazian, A., et al. 2008, *A&A*, 488, 463
- Matteucci, F. 2012, *Chemical evolution of galaxies* (Springer Science & Business Media)
- Miranda, V. P., Tissera, P. B., Sillero, E., et al. 2025, *arXiv e-prints*, arXiv:2511.19630
- Monachesi, A., Gómez, F. A., Grand, R. J. J., et al. 2019, *MNRAS*, 485, 2589
- Mosconi, M. B., Tissera, P. B., Lambas, D. G., & Cora, S. A. 2001, *MNRAS*, 325, 34
- Murphy, G. G., Yates, R. M., & Mohamed, S. S. 2022, *MNRAS*, 510, 1945
- Muñoz-Escobar, I., Tissera, P. B., Gonzalez-Jara, J., et al. 2025, *The mass-metallicity relation of bulges*
- Naidu, R. P., Conroy, C., Bonaca, A., et al. 2022, *arXiv e-prints*, arXiv:2204.09057
- Nomoto, K., Kobayashi, C., & Tominaga, N. 2013, *Annual Review of Astronomy and Astrophysics*, 51, 457
- Panther, B., Jimenez, R., Heavens, A. F., & Charlot, S. 2008, *Monthly Notices of the Royal Astronomical Society*, 391, 1117–1126
- Planck Collaboration, Ade, P. A. R., Aghanim, N., et al. 2014, *A&A*, 571, A16
- Proctor, K. L., Ludlow, A. D., Lagos, C. d. P., & Robotham, A. S. G. 2024, *arXiv e-prints*, arXiv:2407.11444
- Pu, S.-Y., Cooper, A. P., Grand, R. J. J., Gómez, F. A., & Monachesi, A. 2025, *Progenitor diversity in the accreted stellar halos of Milky Way-like galaxies*
- Pulsoni, C., Gerhard, O., Arnaboldi, M., et al. 2020, *Astronomy & Astrophysics*, 641, A60
- Purcell, C. W., Bullock, J. S., & Kazantzidis, S. 2010, *MNRAS*, 404, 1711
- Rey, M. P. & Starkenburg, T. K. 2021, *Monthly Notices of the Royal Astronomical Society*, 510, 4208–4224
- Robertson, B., Bullock, J. S., Font, A. S., Johnston, K. V., & Hernquist, L. 2005, *ApJ*, 632, 872
- Rodríguez, S., García Lambas, D., Padilla, N. D., et al. 2022, *MNRAS*, 514, 6157
- Sanders, R. L., Shapley, A. E., Jones, T., et al. 2021, *ApJ*, 914, 19
- Scannapieco, C., Tissera, P., White, S., & Springel, V. 2005, *MNRAS*, 364, 552
- Scannapieco, C., Tissera, P., White, S., & Springel, V. 2006, *MNRAS*, 371, 1125
- Scannapieco, C., Tissera, P. B., White, S. D. M., & Springel, V. 2008, *MNRAS*, 389, 1137
- Sick, J., Courteau, S., Cuillandre, J.-C., et al. 2015, in *IAU Symposium*, Vol. 311, *Galaxy Masses as Constraints of Formation Models*, ed. M. Cappellari & S. Courteau, 82–85
- Slater, C. T. & Bell, E. F. 2014, *ApJ*, 792, 141
- Smercina, A., Bell, E. F., Price, P. A., et al. 2020, *The Astrophysical Journal*, 905, 60
- Smercina, A., Bell, E. F., Samuel, J., & D’Souza, R. 2022, *ApJ*, 930, 69
- Springel, V. 2005, *MNRAS*, 364, 1105
- Springel, V. & Hernquist, L. 2003, *MNRAS*, 339, 312
- Springel, V., Yoshida, N., & White, S. D. M. 2001, *New A*, 6, 79
- Tapia, B., Tissera, P. B., Sillero, E., et al. 2022, *Boletín de la Asociación Argentina de Astronomía La Plata Argentina*, 63, 256
- Tapia-Contreras, B., Tissera, P. B., Sillero, E., et al. 2025, *Insight into the physical processes that shape the metallicity profiles in galaxies*
- Tau, E. A., Monachesi, A., Gómez, F. A., et al. 2025a, *Astronomy & Astrophysics*, 699, A93
- Tau, E. A., Monachesi, A., Gómez, F. A., et al. 2025b, *Age and metallicity of low-mass galaxies: from their centres to their stellar halos*
- Tinsley, B. M. 1979, *ApJ*, 229, 1046
- Tissera, P., Bignone, L., Gonzalez-Jara, J., et al. 2025, *The CIELO Project: The Chemo-dynamical properties of galaxies and the cosmic web*
- Tissera, P. B., Beers, T. C., Carollo, D., & Scannapieco, C. 2014, *MNRAS*, 439, 3128
- Tissera, P. B., Scannapieco, C., Beers, T. C., & Carollo, D. 2013, *MNRAS*, 432, 3391
- Tissera, P. B., White, S. D., & Scannapieco, C. 2012, *MNRAS*, 420, 255
- Torrey, P., Vogelsberger, M., Marinacci, F., et al. 2019, *Monthly Notices of the Royal Astronomical Society*
- Tremonti, C. A., Heckman, T. M., Kauffmann, G., et al. 2004, *ApJ*, 613, 898
- Trussler, J., Maiolino, R., Maraston, C., et al. 2019, *Monthly Notices of the Royal Astronomical Society*, 491, 5406–5434
- Tsakonas, C., Arnaboldi, M., Bhattacharya, S., et al. 2025, *Astronomy & Astrophysics*, 699, A56
- Vogelsberger, M., Genel, S., Sijacki, D., et al. 2013, *Monthly Notices of the Royal Astronomical Society*, 436, 3031–3067
- Williams, D. J., Damjanov, I., Sawicki, M., et al. 2024, *The Growth of Galaxy Stellar Haloes Over $0.2 \leq z \leq 1.1$*
- Wittig, O., Ramesh, R., & Nelson, D. 2025, *Astronomy & Astrophysics*, 695, A121
- York, D. G., Adelman, J., Anderson, John E., J., et al. 2000, *AJ*, 120, 1579
- Zolotov, A., Willman, B., Brooks, A. M., et al. 2009, *The Astrophysical Journal*, 702, 1058

Appendix A: Cardiograms

We present cardiograms for the remaining 23 stellar halos studied in this article in Fig. A.1. We keep the same labels as Fig. 4. Galaxies are ordered by stellar galaxy mass, with the most massive at the top and the least massive at the bottom. Some cardiograms do not extend to 12 Gyr due to our numerical resolution criterion; values are omitted when this criterion is not met.

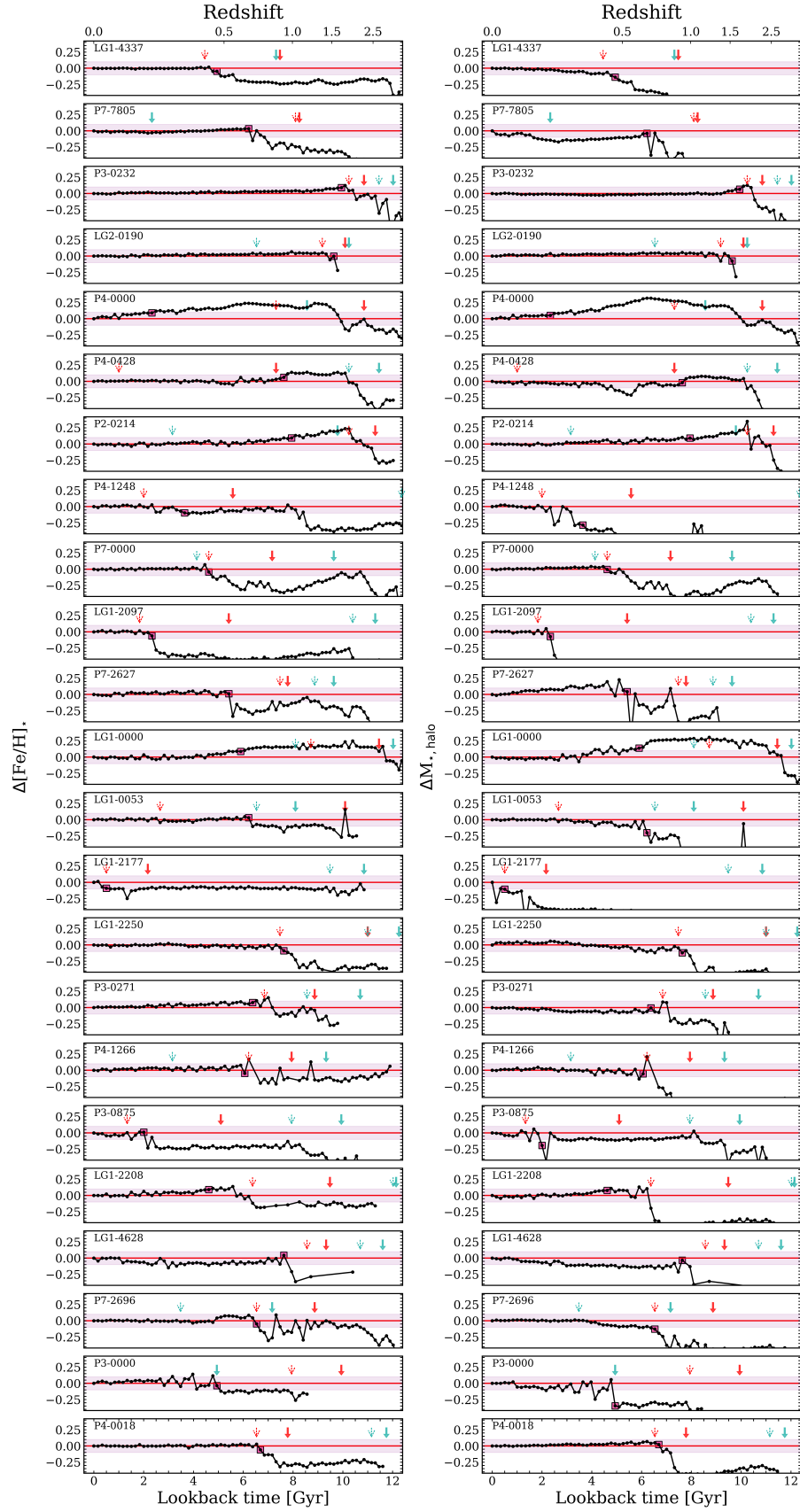


Fig. A.1. Cardiograms for the remaining 23 stellar halos analyzed in this article. Same labels as Fig. 4.